JOURNAL OF GEOPHYSICAL RESEARCH, VOL. 106, NO. D2, PAGES 1569–1581, JANUARY 27, 2001

Relevance of mountain wave cooling for the formation of polar stratospheric clouds over Scandinavia:
Mesoscale dynamics and observations for January 1997

Andreas Dörnbrack and Martin Leutbecher
Institut für Physik der Atmosphäre, Deutschen Zentrum für Luft- und Raumfahrt Oberpfaffenhofen
Wessling, Germany

Jens Reichardt and Andreas Behrendt
GKSS Forschungszentrum, Geesthacht, Germany

Klaus-Peter Müller and Gerd Baumgarten
Physikalisches Institut der Universität Bonn, Bonn, Germany

Abstract. The effect of mesoscale mountain wave–induced temperature anomalies on the formation potential of polar stratospheric clouds above northern Scandinavia is analyzed with a one-month mesoscale model integration. The simulation results are contrasted with synoptic-scale analyses and compared with remote sensing and in situ observations. The mesoscale mass flux of air parcels with temperatures below the threshold for cloud formation through a control volume is compared with its synoptic-scale counterpart. A classification of the synoptic-scale flow into periods of large and small mountain wave activity in the stratosphere is proposed. The derived classification will be used for a climatology of stratospheric mountain wave activity above Scandinavia.

1. Motivation

The depletion of the Arctic stratospheric ozone layer is caused by heterogeneous chlorine activation reactions on particles of polar stratospheric clouds (PSCs) and by halogen-catalyzed destruction due to denitrification of the lower stratosphere [*Carslaw et al.*, 1999]. PSC particles form below a threshold temperature which depends on the mixing ratios of water vapor and nitric acid trihydrate (NAT). The activation of chlorine at PSC particles is very efficient at low temperatures and at high cooling rates because of the growth in particle surface area and the increase of heterogeneous reaction rates [*Peter*, 1997].

Synoptically, minimum stratospheric temperatures are expected to be located close to the center of the polar vortex because of radiative cooling during the polar night. This behavior is predominantly observed over Antarctica. The Arctic stratosphere, however, is frequently disturbed by planetary waves, and the polar vortex is deformed and asymmetric. Currently, the PSC formation potential on the Northern Hemisphere is at best estimated in terms of analyses of global weather prediction models, e.g., the European Centre for Medium-Range Weather Forecasts (ECMWF) analyses. The Norwegian Institute for Air Research (NILU) provides products based on T106 L31 (horizontal resolution of 1.125° × 1.125° and 31 vertical levels) ECMWF analyses of the recent winters via internet for the "European ozone community" (available at http://www.nilu.no/avd/reg-glo/nadir/nadir.html). Climatological time series of stratospheric minimum temperatures based on such or similar data sources, e.g., *Pawson et al.* [1995] and National Centers for Environmental Prediction (NCEP) [*Coy et al.*, 1997], show that the Arctic stratosphere is often too warm for PSC formation. The Berlin group offers their database of geopotential heights and temperatures in the stratosphere via http://strat-www.met.fu-berlin.de; a complete set of meteorological information of the stratospheric state is available via the internet site of the NCEP at http://www.ncep.noaa.gov.

Recent observations and modeling studies give evidence that the formation of solid PSC particles in the Arctic can be triggered by mesoscale meteorological processes leading to stratospheric temperature anomalies [*Carslaw et al.*, 1998a, b]. In particular, topographically excited gravity waves are able to propagate up to stratospheric levels. There, the adiabatic cooling of air parcels moving along vertically displaced isentropes controls mesoscale temperature anomalies and the associated occurrence of mountain wave–induced PSCs.

Carslaw et al. [1999] have shown that episodes of wave-induced cooling have major effects on PSC microphysics and chemistry. Thus the formation of mountain wave–induced PSCs can lead to an additional ozone depletion over the Arctic that is not accounted for in global chemical transport models [*Knudsen*, 1997; *Carslaw et al.*, 1998a]. Furthermore, the microphysical interpretation of particular observations as well as a reliable estimate of the total hemispheric ozone loss require an understanding about mesoscale stratospheric temperature anomalies.

Mountain wave–induced PSCs are of smaller spatial extent (typical horizontal wavelength of ≈350 km) and of shorter lifetime (~6 hours) compared to their synoptic-scale counterparts. Thus the following questions arise: How relevant are these clouds for the stratospheric ozone budget? How often do they occur? How much air is additionally processed in heter-

Paper number 2000JD900194.
0148-0227/01/2000JD900194$09.00

ogeneous reactions in mountain wave–induced PSCs related to synoptic-scale estimates? Here, a one-month mesoscale model integration is presented to analyze the effect of mountain wave–induced temperature anomalies on the formation potential of PSCs and to provide necessary input from mesoscale dynamics to answer these questions for northern Scandinavia.

Recent papers have shown that mesoscale numerical simulations of flow across mountains represent observed stratospheric temperature anomalies for particular cases fairly well [*Dörnbrack et al*., 1999; *Wirth et al*., 1999; *Leutbecher and Volkert*, 2000]. Mesoscale simulations are able to resolve the orographic features of the mountain ridges much better than global models because of the limited area considered in such studies. This essentially leads to a more realistic spectrum of horizontal wavenumbers and to greater amplitudes of the orographically induced gravity waves. Furthermore, a large number of vertical levels better resolves the vertical wave propagation.

A particular case study is rarely representative for an ensemble of all possible realizations. On the other hand, mesoscale modeling even on the fastest supercomputers is too expensive and too time-consuming to cover the spatial and temporal range of interest, i.e., the whole Arctic during the recent winter seasons. In January 1997 several coordinated European field campaigns (cf. *Harris et al*. [1998] for preliminary results of Airborne Polar Expedition–Polar Stratospheric Clouds, Lee Waves, Chemistry, Aerosols and Transport (APE-POLECAT), Stratospheric Aerosols and Ozone in the Northern and Southern Hemispheres (SAONAS), LEEWAVE, etc.) took place in northern Scandinavia, aiming inter alia at PSC observations. Therefore January 1997 was chosen for the one-month integration of the flow over the Scandinavian mountain range. This is the longest simulation we can afford at a spatial resolution sufficient to study the effects of this mountain range.

Obviously, even results of a prolonged, one-month case study for Scandinavia cannot easily be applied to other years and other locations. Therefore simple and reliable parameterizations of stratospheric temperature anomalies, e.g., based on linear wave theory [*Bacmeister et al*., 1994, 1999], are necessary to investigate the hemispheric influence of mountain wave–induced PSCs on a climatological scale. These parameterizations have open parameters that need to be adjusted. The sparse observational network does not allow this adjustment. Thus a more reliable link between observations and parameterizations is required. It can be provided by the mesoscale simulation presented in this study.

Here, dynamical criteria of stratospheric mountain wave activity are deduced, and this parameterization is compared with mesoscale model results. In the companion paper these criteria are employed to estimate the climatological relevance of mountain wave cooling for PSC formation above Scandinavia during the recent 20 years [*Dörnbrack and Leutbecher*, this issue].

The paper is organized as follows: ECMWF analyses are utilized to characterize the synoptic-scale stratosphere over Scandinavia. This data set and details of the mesoscale model simulation are described in section 2. In section 3, the stratospheric minimum temperatures of both data sets are compared for January 1997. As a first approach to compare simulated minimum temperatures with observations, time series of PSCs observed in the lee of the Scandinavian mountains by ground-based lidar systems are utilized. Second, the model results are compared with radiosonde data of Sodankylä, Finland. The question "How much air is additionally processed by heterogeneous reactions in mountain wave–induced PSCs?" will be answered in section 4. Criteria of stratospheric wave activity are presented in section 5. In section 6, the relationship between the position of the polar vortex and mountain wave activity will be discussed. This paper is concluded in section 7 with a summary of the results.

2. Database

Daily ECMWF analyses serve to characterize the synoptic-scale state of the atmosphere. The 6-hourly data are stored on a regular latitude-longitude grid with a spatial resolution of 1.125° and with 31 model levels from the surface to 10 hPa (T106 L31 model resolution).

The mesoscale fields for January 1997 are calculated with the nonhydrostatic weather prediction model MM5 [*Dudhia*, 1993; *Grell et al*., 1994]. The model domain is centered around (65°N, 15°E) with an extension of 2745 km × 2745 km. A local grid refinement (nested domain of 1590 km × 1590 km) covers Scandinavia almost entirely (Figure 1). The nested domain is used to resolve most of the spectrum of vertically propagating gravity waves generated by the orography. The horizontal mesh size of the outer domain is $\Delta x = 45$ km, and the grid length of the nested domain amounts to 15 km. Terrain heights on the 15 km grid were obtained by interpolation from a 30″ orographic data set provided by the Geophysical Data Center (Boulder, Colorado).

The vertical resolution amounts to approximately 0.6 km. In total, 52 levels are used up to the model top at 10 hPa (≈28 km). At the upper boundary a radiation condition avoids the reflection of vertically propagating gravity waves. Radiative and moist processes are switched off as the prime concern lies in the dynamics of mountain waves at upper levels. The initial conditions and boundary values of the model integration were prescribed by 12-hourly analyses of the ECMWF with a horizontal resolution of 2.5° in latitude and longitude and 15 levels between the surface and the 10 hPa pressure level [see *Dörnbrack et al*., 1998].

The one-month integration is split into 15 periods, each 60 hours long. The individual simulations start at $t_{\text{init}} = 1200$ UT every other day beginning on January 1, 1997. For the analysis, results from the last 48 hours of every simulation ($t_{\text{init}} + 12$ hours until $t_{\text{init}} + 60$ hours) are used. The three-dimensional data fields are archived every 3 hours, and they are available for use by other groups. The total integration consumed approximately 160 CPU days on CRAY J90.

3. Minimum Temperatures and PSC Formation

The synoptic-scale and mesoscale model minimum temperatures T_{min} at 100, 70, 50, and 30 hPa above Scandinavia for January 1997 are plotted in Figure 2. Essentially, the time series of T_{min} for this month can be divided into four phases: A pronounced early cooling until January 3 is followed by a period of weak temperature oscillations (±3 K in 10 days) until January 15. Afterward, a remarkable cooling takes place with an absolute temperature minimum around January 21. Finally, at the end of the month a sudden warming (approximately equal to +15 K/5 days) terminates the cold interval.

For a given mixing ratio of water vapor and nitric acid, PSCs form if the local temperature falls below a threshold value [*Hanson and Mauersberger*, 1988]. PSCs are classified in two

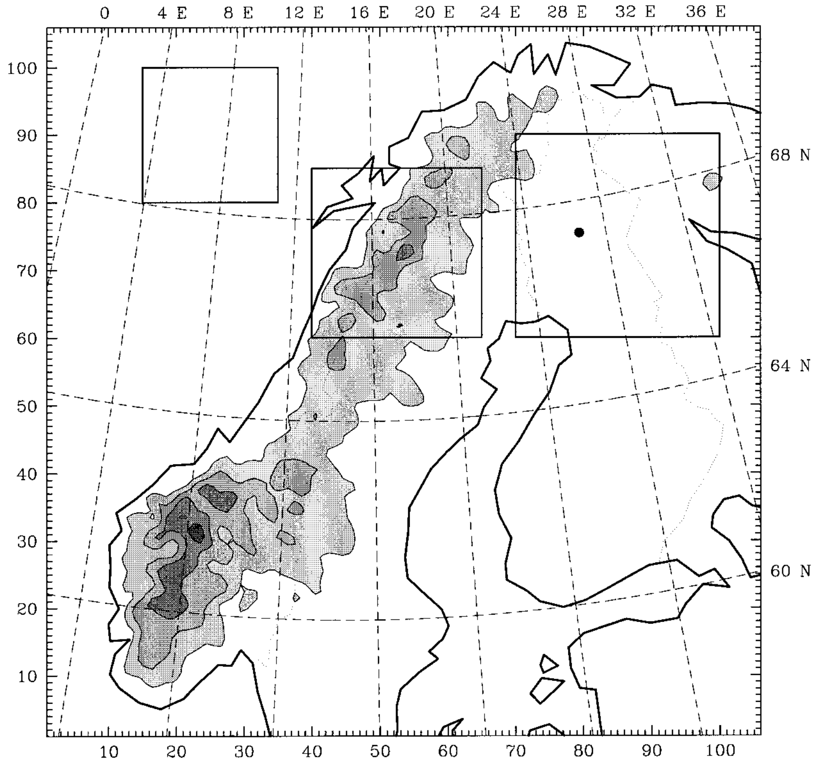

Figure 1. Model orography of Scandinavia in the nested computational domain. Contour lines of the terrain height are every 400 m, starting at 400 m. The boxes designate three control areas, from west to east: "Norwegian Sea," "Kebnekaise," and "Sodankylä," respectively. Tick marks on the perimeter indicate the grid spacing of 15 km.

main groups: PSCs of type II consist of water ice particles, form at temperatures ~4 K below the ice frost point T_{frost}, and are identical to the mother-of-pearl clouds; PSCs of type I exist at higher temperatures and consist of nitric acid trihydrate (NAT), where T_{NAT} is the existence temperature of type I PSCs (for a recent discussion of the PSC classification, see *Stein et al.* [1999]).

By cursory inspection of Figure 2 the temporal evolution of the mesoscale T_{min} is quite similar to that of the ECMWF analyses. A detailed comparison reveals that the mesoscale simulation results reach lower absolute values. During the cold period, T_{min} falls below the frost point T_{frost} of water ice (at the uppermost pressure level, by more than 5 K); synoptic-scale temperatures never reach the frost point. Furthermore, mesoscale results support the formation of PSCs (i.e., periods when $T_{\mathrm{min}} < T_{\mathrm{NAT}}$ or $T_{\mathrm{min}} < T_{\mathrm{frost}}$) for longer times. Even in periods when the stratosphere tends to become synoptically warmer, mesoscale processes reduce temperatures by 4–5 K below the threshold (see period from January 7 till 9 in Figure 2).

In order to quantify the effects of mountain wave cooling in the stratosphere the difference between the synoptic-scale and mesoscale minimum temperature T_{min} is determined for two distinct control areas. The first box is located above the "Norwegian Sea," and the other is located directly above the highest mountain of northern Scandinavia "Kebnekaise" (67°54′N, 18°30′E, see Figure 1). The temperature difference $\Delta T = \Delta T_{\mathrm{min}} - \Delta \bar{T}$, where $\Delta T_{\mathrm{min}} = T_{\mathrm{min}}^{\mathrm{MM5}} - T_{\mathrm{min}}^{\mathrm{T106}}$ is the actual difference between the minimum temperatures at a given time, takes into account that the area-averaged temperatures $\bar{T}$ in the control areas can be different ($\Delta \bar{T} = \bar{T}^{\mathrm{MM5}} - \bar{T}^{\mathrm{T106}} \neq 0$).

Upstream of the mountain range the temperature minimum anomaly ΔT is close to zero, and only random deviations of less than 2 K occur (Figure 3a). Large mesoscale temperature anomalies $\Delta T < 0$ exclusively appear above and downstream from the mountain range (Figure 3b). There, absolute values of $\Delta T > 2$ K are calculated in periods of stratospheric mountain wave activity (its parameterization is employed in section 5). In these periods the temperature decreases simultaneously at all stratospheric levels. However, maximum values of $\Delta T \approx 8$ K are solely present at the highest stratospheric level of 30 hPa considered here. Three marked periods of maximum ΔT exist, namely on January 9–10, 15–16, and 21–22.

Direct observations of mesoscale mountain wave cooling in the stratosphere are rare and restricted to singular case studies [e.g., *Gary*, 1989; *Schreiner et al.*, 1999]. A first step to compare simulated mesoscale minimum temperatures with measurements is to use records of observed PSCs. Thus their existence indicates regions of stratospheric temperature below the threshold values of T_{NAT} and T_{frost}. Here, PSC records of two ground-based lidars at Esrange (67.88°N, 21.06°E), the University of Bonn backscatter lidar [see *Müller et al.*, 1998] and the GKSS Raman lidar [*Reichardt et al.*, 1996] are considered (Plate 1). Because their properties differ in detail (lidar wavelength; ability to measure under daylight conditions), both lidars complement one another. Additionally, the ice PSC observation by airborne lidar on January 9, 1997 [*Wirth et al.*, 1999], is superimposed on Plate 1.

Plates 1a and 1b summarize the evolution of different PSC types as observed over Esrange. The PSC types are classified by the backscatter ratio S ($S = (\beta_{\mathrm{aerosol}} + \beta_{\mathrm{air}})/\beta_{\mathrm{air}}$, where β is the backscatter coefficient at 532 nm in the parallel channel)

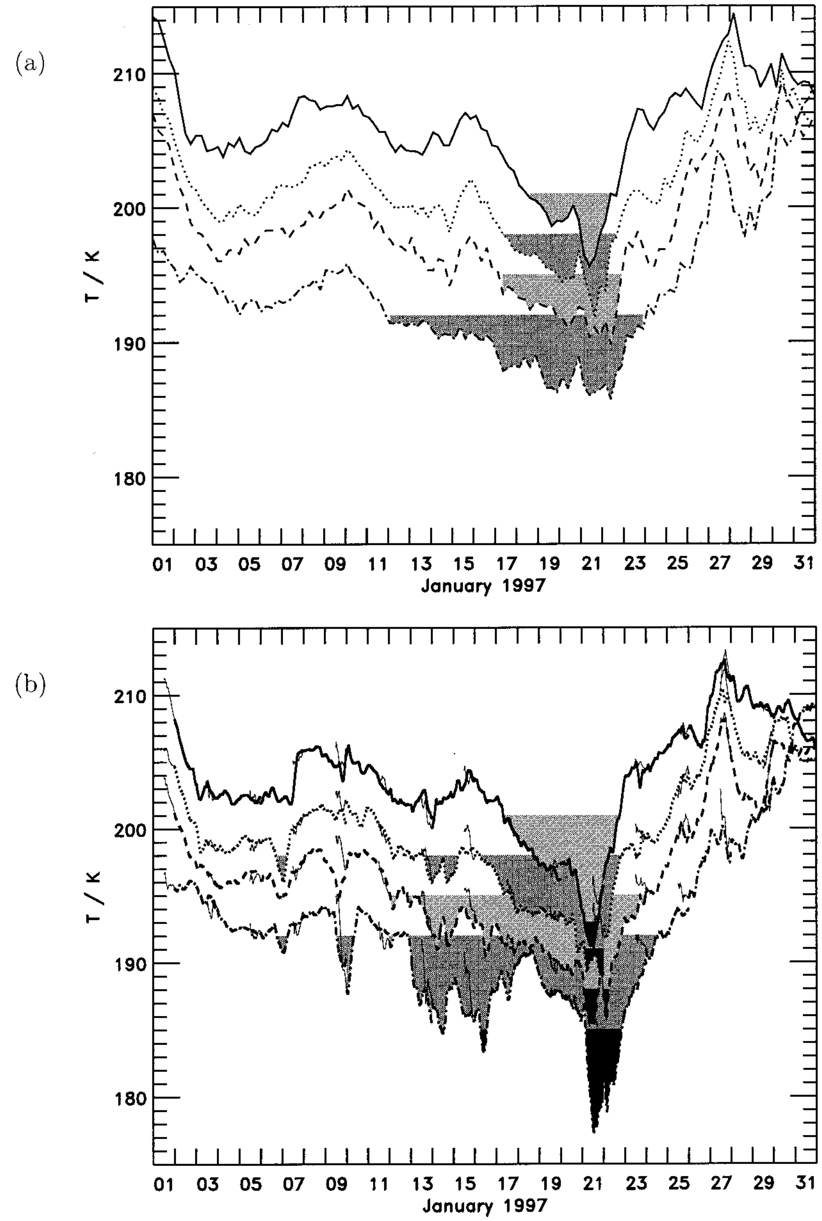

Figure 2. Synoptic-scale versus mesoscale minimum temperatures above Scandinavia as shown in Figure 1 during January 1997. (a) Synoptic-scale minimum temperatures from 6-hourly ECMWF analyses at T106 L31 resolution. (b) Mesoscale minimum temperatures at $\Delta x = 15$ km resolution every time step (30 s). Data are plotted at 100 (solid lines), 70 (dotted lines), 50 (dashed lines), and 30 hPa (dash-dotted lines). Thin solid segments in Figure 2b mark the first 12 hours of mesoscale simulations, and thick segments mark the following 48 simulation hours. Shaded areas mark periods where $T < T_{\mathrm{NAT}}$ (grey) and $T < T_{\mathrm{frost}}$ (black). The PSC formation temperatures T_{NAT} and T_{frost} are calculated assuming volume mixing ratios of 5 ppm for water vapor and 10 ppb for nitric acid trihydrate (NAT) [*Hanson and Mauersberger*, 1988].

and the aerosol depolarization δ ($\delta = \beta_{\perp}/\beta_{\|}$, where $\beta_{\perp}$ is the aerosol backscatter coefficient for cross polarization and $\beta_{\|}$ is the aerosol backscatter coefficient for aligned polarization at 532 nm) as proposed by *Poole and McCormick* [1988] and *Browell et al.* [1990]: that is, PSC of type II, large S and δ; PSC of type Ib, small S and negligible δ; and PSC of type Ia, small S and large δ. In Plate 1 no information about the magnitude in terms of S of the individual PSC events is given.

Although the lidar measurements were frequently hindered because of poor tropospheric transmittivity, the overall temporal coverage of the PSC records is fairly good in January 1997. During the synoptically warm period ($T_{\min} > T_{\mathrm{NAT}}$) until January 12, the observed PSCs of type I are exclusively caused by mesoscale cooling in the stratosphere. Especially, the ice PSC on January 9 directly above the highest mountains west of Esrange gives evidence for the localized cooling by mountain waves [*Wirth et al.*, 1999]. During the synoptically cold interval ($T_{\min} < T_{\mathrm{NAT}}$) from January 13 till 23, mountain wave cooling modulates the stratospheric temperature above the control area "Kebnekaise" significantly in two periods around January 16 and 22 (see Figure 3). Only in these periods were PSCs of type II observed by the ground-based lidars. As

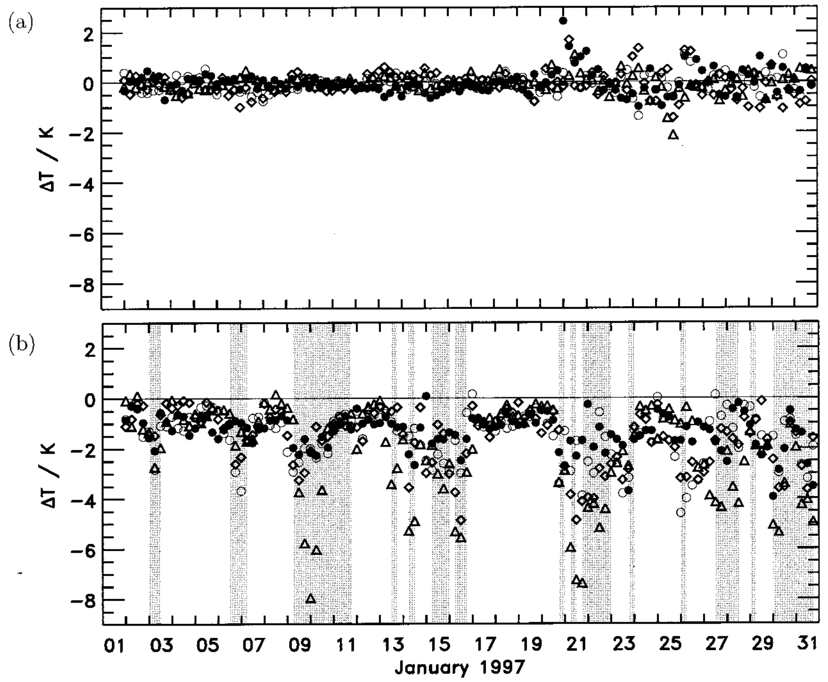

Figure 3. Temperature minimum anomaly $\Delta T = \Delta T_{\min} - \Delta \bar{T}$ at 100 (solid circles), 70 (open circles), 50 (diamonds), and 30 hPa (triangles). The values of $\Delta T_{\min}$ and $\Delta \bar{T}$ are calculated as $T^{\mathrm{MM5}}_{\min} - T^{\mathrm{T106}}_{\min}$ and $\bar{T}^{\mathrm{MM5}} - \bar{T}^{\mathrm{T106}}$, where the temperatures $\bar{T}$ are averages over the individual control areas (a) Norwegian Sea and (b) Kebnekaise. Periods where the simple parameterization (compose Figure 8) indicates significant mountain waves in the stratosphere are shaded.

the synoptic-scale temperature analyses were always above the frost point, the occurrence of ice PSCs confirms the simulated mesoscale results that predict mountain wave cooling with $T_{\min} < T_{\mathrm{frost}}$. At the end of the month no PSCs have been observed because the sudden stratospheric warming destroyed the favorable conditions for PSC formation. Thus even large mesoscale cooling ΔT cannot lower the temperatures below the threshold values. Temperature profiles of the Esrange radiosonde on the last 3 days of the month show pronounced wavelike structures with amplitudes of up to 7 K and confirm the simulated gravity wave activity.

A direct validation of the simulated stratospheric temperature field with radiosonde observations during the complete January 1997 is only possible at Sodankylä (Figure 4); other stations (Bodø, Andøya, Kiruna) cannot regularly provide data for altitudes aloft 100 hPa. At Sodankylä, radiosondes are routinely launched every 12 hours; together with additional soundings (as backscatter or ozonesondes) there are 65 ascents in January 1997. Although the number of observations decreases with height (21% of all balloons reached levels higher than 15 hPa in contrast to 83% at 50 hPa), the high–vertical resolution soundings constitute a valuable data set [see *Gaffen*, 1994]. Frequently, the radiosonde balloons are advected up to 250 km downstream from Sodankylä because of the strong tropospheric and stratospheric winds.

For the case studies of January 9 and 22 [*Wirth et al.*, 1999; *Dörnbrack et al.*, 1999] a close agreement between the simulated and observed stratospheric temperature was attained by calculating the simulated temperature at the actual trajectory of the balloon. In order to evaluate the overall model performance in January 1999 we compare the observed temperature values with the simulated extremum temperatures in the vicinity of Sodankylä. This approach emphasizes potential amplitude errors and neglects potential phase errors of the numerical model. The control area "Sodankylä" is suitable as it is just large enough to cover all trajectories of sondes launched at Sodankylä. It turns out that most of the observed values fall into the range between the simulated minimum and maximum temperatures (Figure 4). In some instances the observed temperature is identical to a simulated extreme value [see *Kivi et al.*, 1998]. This result suggests that the numerical model neither grossly overestimates nor underestimates the amplitude of the waves present over "Sodankylä."

Large differences between minimum and maximum temperature of up to 20 K inside the control area indicate large horizontal temperature gradients. Although ~500 km downwind of the mountain ridge, these gradients are associated with hydrostatic mountain waves with horizontal wavelengths larger than 300 km. These waves are inertia gravity waves. Their propagation is influenced by the Coriolis force, and they propagate energy at a slant angle [*Queney*, 1948]. This results in vertical displacements of isentropic surfaces several hundred kilometers downstream of the ridge crest [*Dörnbrack et al.*, 1999].

Summarizing, the simulated stratospheric temperature field is perturbated by mountain waves with a horizontal wavelength of $\lambda \sim 100$ km and larger. The comparison with observations suggests that the amplitude of these perturbations is quite realistic. The simulated stratospheric fields are used in section 4 to estimate the influence of mesoscale mountain wave activity on the PSC formation and the consequent processing of air in heterogeneous reactions.

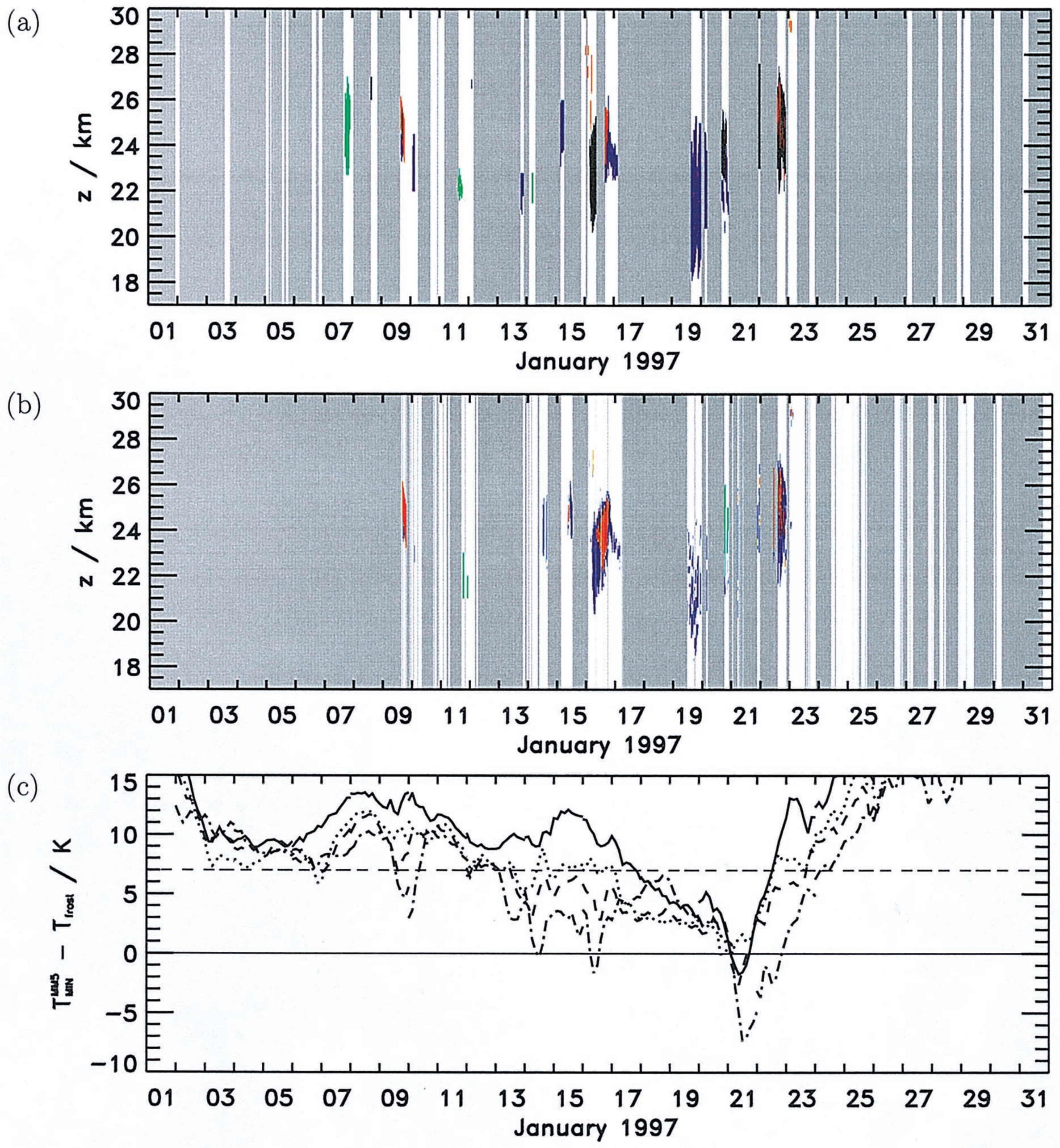

Plate 1. Time-altitude plot of PSC observations by lidars at Esrange, Kiruna (67.88°N, 21.06°E), in January 1997. (a) GKSS Raman lidar. (b) University of Bonn backscatter lidar. Observational periods of each lidar system are marked by white background. Color coding is as follows: PSC of type II; blue, PSC of type Ib; green, PSC of type Ia; black, not PSC type Ia, Ib, or II. Additionally, the PSC of type II observed on January 9, 1997, by the airborne lidar of the DLR Falcon is drawn in red. (c) Temperature difference $T_{\mathrm{min}}^{\mathrm{MM5}} - T_{\mathrm{frost}}$ at 100 hPa (solid line), 70 hPa (dotted line), 50 hPa (dashed line), and 30 hPa (dash-dotted line) above control area Kebnekaise. The dashed line at 7 K refers to $T_{\mathrm{min}}^{\mathrm{MM5}} - T_{\mathrm{NAT}} = 0$.

4. Processing of Air in Heterogeneous Reactions

The previous analysis has shown that minimum temperatures due to mesoscale mountain waves are up to 8 K lower than the minimum temperatures of synoptic-scale analyses in the same area. This may lead to the formation of mountain wave–induced PSCs. However, the relevance of these additional PSCs to the stratospheric ozone budget remains unclear as the mountain wave–induced clouds may be small in comparison to their synoptic-scale counterparts. In order to quantify the relevance of mountain wave–induced PSCs we now calculate the amount of air processed by heterogeneous reactions by comparing synoptic-scale analyses on the one hand and the mesoscale simulation results on the other hand. This quantifies how much air is being processed because of the presence of mountain waves, which are well represented in the mesoscale simulations and almost absent in the synoptic-scale analyses.

The rate at which heterogeneous reactions transform the trace constituents relevant to the ozone budget critically de-

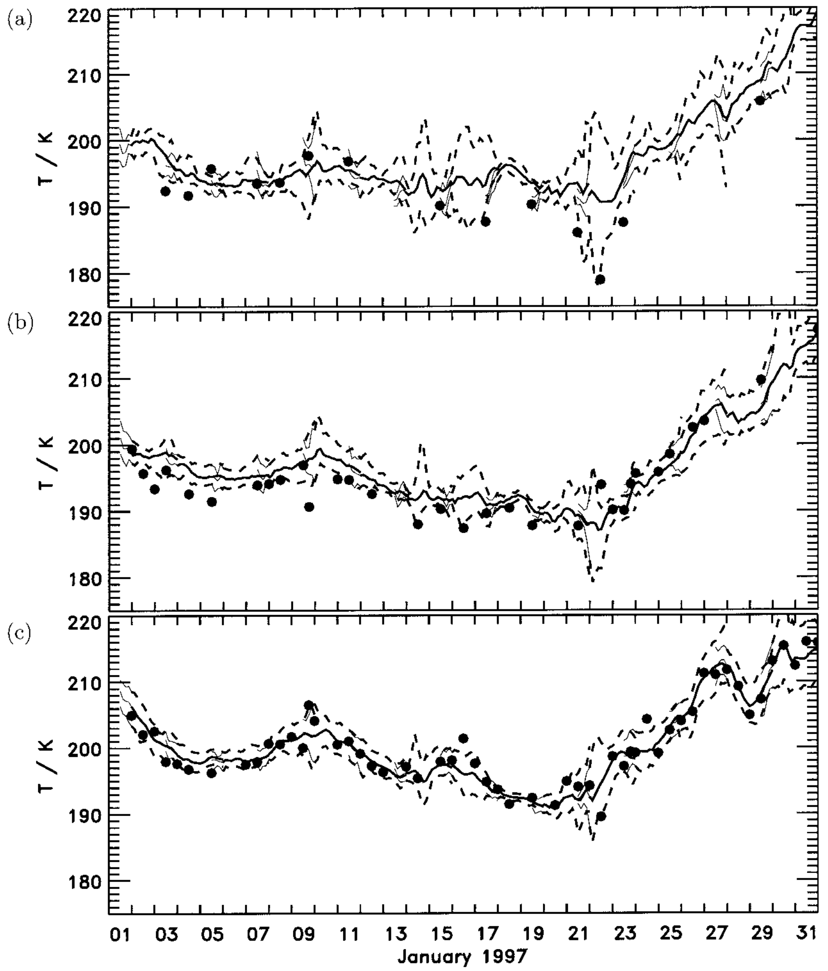

Figure 4. Mean (solid lines) and minimum-maximum (dashed lines) model temperatures in control area Sodankylä at (a) 15, (b) 28, and (c) 50 hPa in January 1997. Solid circles mark measurements by the Sodankylä radiosonde at the same levels. Thin solid line segments mark the first 12 hours of mesoscale simulations, and thick segments mark the following 48 simulation hours.

pends on temperature. When the temperature is too high, no PSC particles form at all. If the temperature is below $T_{\mathrm{frost}} -$ 4 K, ice particles grow quickly and provide a large particle surface area. At such temperatures all chlorine available can be converted to active compounds on the order of 10 min [*Carslaw et al.*, 1998a].

This behavior suggests that the microphysics of PSC formation and the subsequent processing due to heterogeneous reactions can be idealized in the form of a temperature-dependent on/off switch. At temperatures higher than a threshold temperature T_*, no processing, and below T_*, complete processing, takes place. A good choice of the threshold value T_* depends on details of the microphysics and the heterogeneous reaction rates. We consider several threshold temperatures rather than trying to specify an optimal value. The values $T_* = T_{\mathrm{NAT}}$, $T_{\mathrm{NAT}} \pm 2$ K, T_{frost}, and $T_{\mathrm{frost}} \pm 2$ K have been chosen, where T_{NAT} and T_{frost} depend on pressure and assumed volume mixing ratios of 5 ppm for water vapor and 10 ppb for nitric acid trihydrate [*Hanson and Mauersberger*, 1988]. This range of threshold temperatures is thought to represent the inaccuracy of the present knowledge of the microphysics as well as a temperature bias of the synoptic-scale analyses or variations of the water vapor or nitric acid mixing ratios.

In the following, we consider the processing of air within the control volume Kebnekaise. Every n hours a set of 2500 trajectories is released at the lateral boundaries of the control volume at 25 model levels between 85 and 15 hPa. On the basis of a typical timescale over which the flow changes, we set $n = 12$ for the synoptic-scale flow and $n = 3$ for the mesoscale flow. The spacing of the starting locations of the trajectories is equal to the horizontal and vertical grid spacings Δx and Δz of the model.

The subset of trajectories entering the control volume at the initial time t_0 is called Z. Each trajectory $\tau \in Z$ can be thought of as being associated with a mass flux $[\rho v_\perp \Delta x \Delta z]_{\tau,t_0}$, where ρ is the density and $v_\perp$ is the velocity component normal to the boundary at the initial time t_0 at the starting point of trajectory τ. The entire mass flux into the control volume above 85 hPa and below 15 hPa is then given by

$$I = \sum_{\tau \in Z} [\rho v_\perp \Delta x \Delta z]_{\tau,t_0}.$$

Let $Z^{(p)}(T_*)$ be the subset of Z of those trajectories that encounter a temperature below the threshold temperature T_* on their passage through the control volume. Then the mass

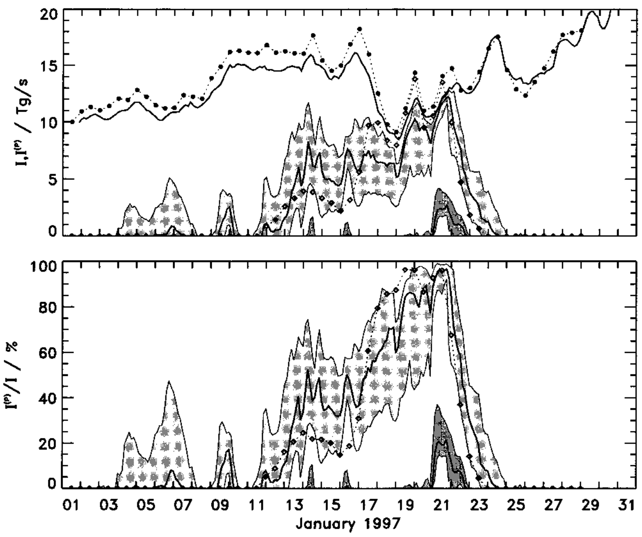

Figure 5. Mass flux in the layer between 85 and 15 hPa through the control volume Kebnekaise. (top) Total mass flux from mesoscale simulations (solid lines) and from ECMWF analyses (dotted line with solid circles). Mass flux of air processed by heterogeneous reactions: ECMWF analyses $T_* = T_{\mathrm{NAT}}$ (dotted line with diamonds), mesoscale model $T_* = T_{\mathrm{NAT}} \pm 2$ K (light grey shading), and mesoscale model $T_* = T_{\mathrm{frost}} \pm 2$ K (dark grey shading). (bottom) Relative mass fluxes related to the total mass fluxes and coded as above.

flux of air which is being processed by heterogeneous reactions will be given by

$$I^{(p)}(T_*) = \sum_{\tau \in Z^{(p)}(T_*)} [\rho v_\perp \Delta x \Delta z]_{\tau,t_0}.$$

In a curved flow a trajectory may leave the control volume and reenter it later on. However, only those trajectories that are processed on the first passage through the control volume are considered because a trajectory reentering the volume is already represented by another trajectory starting at the location of the reentrance.

The evolution of the total and the processed mass fluxes in January 1997 is plotted in Figure 5. The total mass flux in the layer between 85 and 15 hPa through the control volume Kebnekaise ranges from 10 to 20 × 10^9 kg s^{-1}. For westerly flow this corresponds to a mean wind speed of 14–28 m s^{-1} and, for northwesterly flow, to 19–38 m s^{-1}. The change of the total mass flux is correlated with the position of the control volume with respect to the polar vortex. At the edge of the vortex the mass flux is higher because of the strong westerly polar night jet whereas in the center of the polar vortex (January 17–19) the mass flux becomes smaller.

When the synoptic-scale temperature is a little above the threshold value ($T - T_* < 5$ K), mountain waves can induce increased processing of air. During the period January 3–11 this happens for a threshold value around T_{NAT}. There is no processing at $T < T_{\mathrm{NAT}}$ due to the synoptic-scale flow, but up to 15 % of the total mass flux is processed on the mesoscale. The result for a threshold value around T_{frost} is even more pronounced. During the entire January 1997 no synoptic-scale processing at $T < T_{\mathrm{frost}}$ occurs in the control volume. However, the mass flux of air processed on the mesoscale reaches up to 20% of the total flux. This is due to the large-amplitude mountain wave event on January 21–22.

The mass flux of processed air proves to be quite sensitive to the threshold value T_*. For instance, on January 6–7, 1997, the mass flux $I^{(p)}(T_*)$ increases from 7 to 46% of I when the threshold value $T_* = T_{\mathrm{NAT}}$ is increased by 2 K. The sensitivity at $T_* \approx T_{\mathrm{frost}}$ during the event on January 21–22 is somewhat weaker but still large. At the maximum of processing, $I^{(p)}$ varies from 13 to 35% for T_* ranging from $T_{\mathrm{frost}} - 2$ K to $T_{\mathrm{frost}} + 2$ K.

Data such as ΔT and $I^{(p)}(T_*)/I$ of the one-month mesoscale integration of January 1997 can be used to test parameterizations of mountain wave cooling. As mentioned in section 1, these parameterizations are currently the only means to estimate the effect of mountain waves on the hemispheric ozone budget in the stratosphere. In section 5, dynamical criteria for stratospheric mountain wave activity are presented. This is a step to build a simple parameterization of stratospheric mountain wave cooling that is employed in the companion paper to obtain a climatology [*Dörnbrack and Leutbecher*, this issue].

5. Criteria for Stratospheric Mountain Wave Activity

Early observations of mother-of-pearl clouds in northern Scandinavia reveal a strong correlation between their appearance during the polar night and deep surface pressure lows passing the Norwegian Sea toward the northeast [*Mohn*, 1893; *Störmer*, 1931, 1934]. For example, *Dietrichs* [1950] analyzed

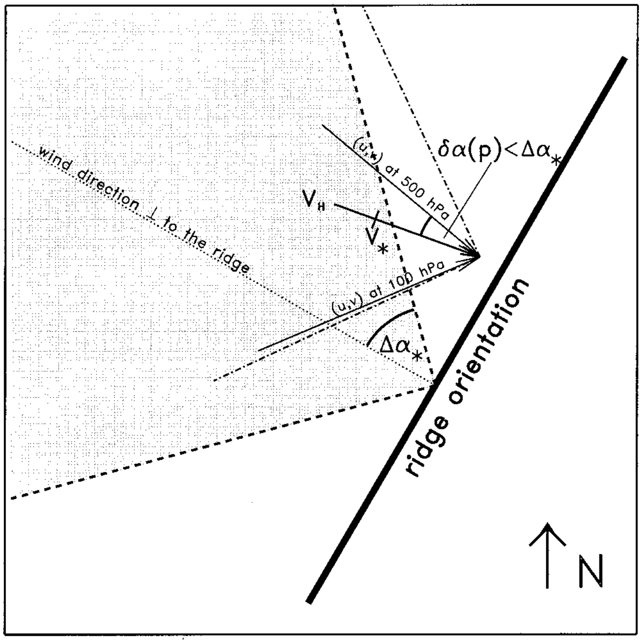

Figure 6. Schematic sketch of criteria C1 ($V_H > V_*$), C2 ($300° - \Delta\alpha_* < \alpha_H < 300° + \Delta\alpha_*$), and C3 ($\delta\alpha(p) = \alpha_H(p) - \alpha_H < \Delta\alpha_*$, p = 500, 300, 100, 50 hPa), where V_H and α_H are the horizontal wind speed and direction at 900 hPa, of the simple mountain wave parameterization. The ridge orientation corresponds to that of the Scandinavian mountain range.

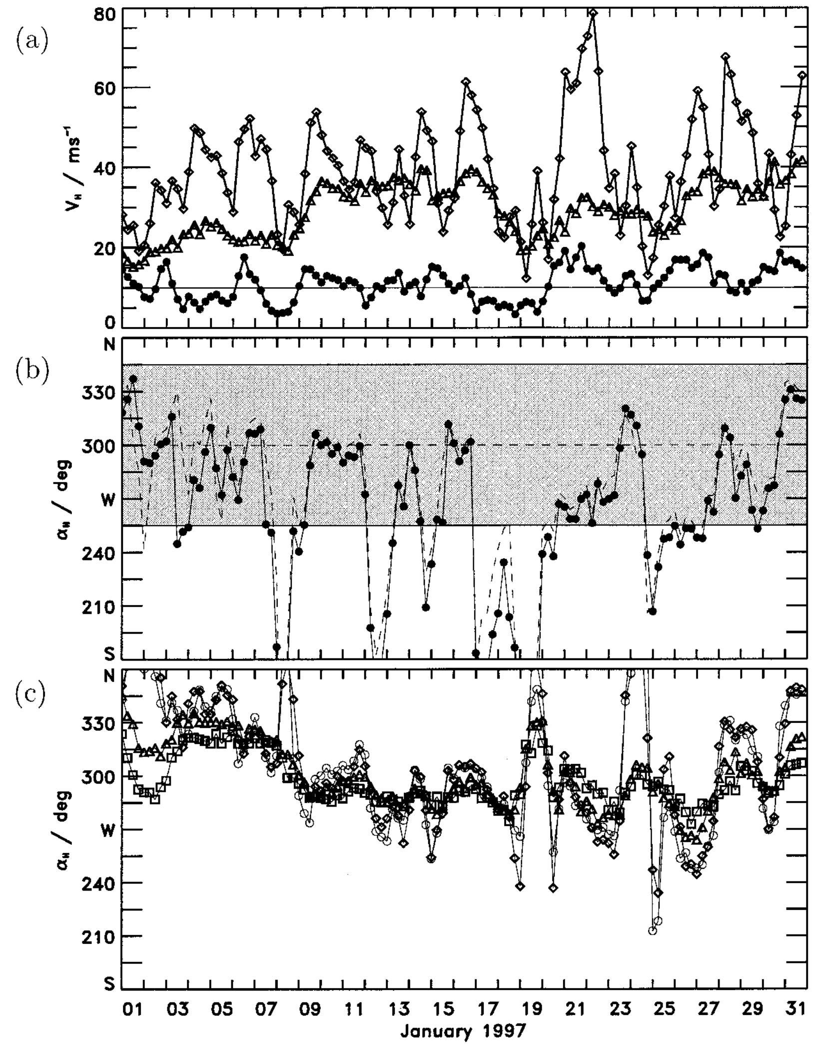

Figure 7. Area-averaged synoptic-scale horizontal wind speed V_H and wind direction α_H in control area Kebnekaise during January 1997. (a) Magnitude of the horizontal wind vector V_H at 900 (solid circles), 300 (diamonds), and 100 hPa (triangles). (b) Wind direction α_H at 900 (solid line with circles) and 850 hPa (dashed line with circles). The shaded area marks the segment where the wind is nearly normal to the mountain crest. (c) Wind direction α_H at 500 (circles), 300 (diamonds), 100 (triangles), and 50 hPa (squares). Averages are taken from 6-hourly ECMWF T106 L31 analyses.

systematically 96 observations from a 60 year period. He concluded that in more than 75% of all records the low-level wind speed on the upstream side was high and the wind direction was west-northwest. Furthermore, he classified mother-of-pearl clouds as mountain clouds; that is, they can be considered as the stratospheric relatives of lenticularis clouds frequently observed simultaneously in the troposphere.

The aim of this section is to deduce simple dynamical criteria to determine when significant gravity waves are forced by airflow over the Scandinavian mountain range and when they influence the stratospheric flow. For this purpose, we consider the flow over an elongated mountain range and assume that the air is stably stratified throughout the troposphere and stratosphere (Figure 6). For a given terrain height the magnitude of the velocity component perpendicular to the mountain ridge determines how much energy is transferred to vertical oscillations. Therefore we assume criteria C1 and C2 as follows:

1. According to criterion 1 (C1) the horizontal wind speed V_H at 900 hPa must be larger than a threshold value V_*:

$$V_H > V_*.$$

2. According to criterion 2 (C2) the wind direction α_H at 900 hPa should not deviate more than $\Delta\alpha_*$ from the normal of the mountain ridge (for Scandinavia 300°, see Figure 6):

$$300° - \Delta\alpha_* < \alpha_H < 300° + \Delta\alpha_*.$$

For small values of $\Delta\alpha_*$ and large V_* the preceding conditions assure a significant forcing of mountain waves. The next criterion, C3, demands that the propagating mountain waves transport most of their energy to stratospheric levels without considerable loss, e.g., by wave absorption at critical levels [cf. *Whiteway and Duck*, 1996; *Dörnbrack*, 1998].

3. According to criterion 3 (C3) the upper level winds do

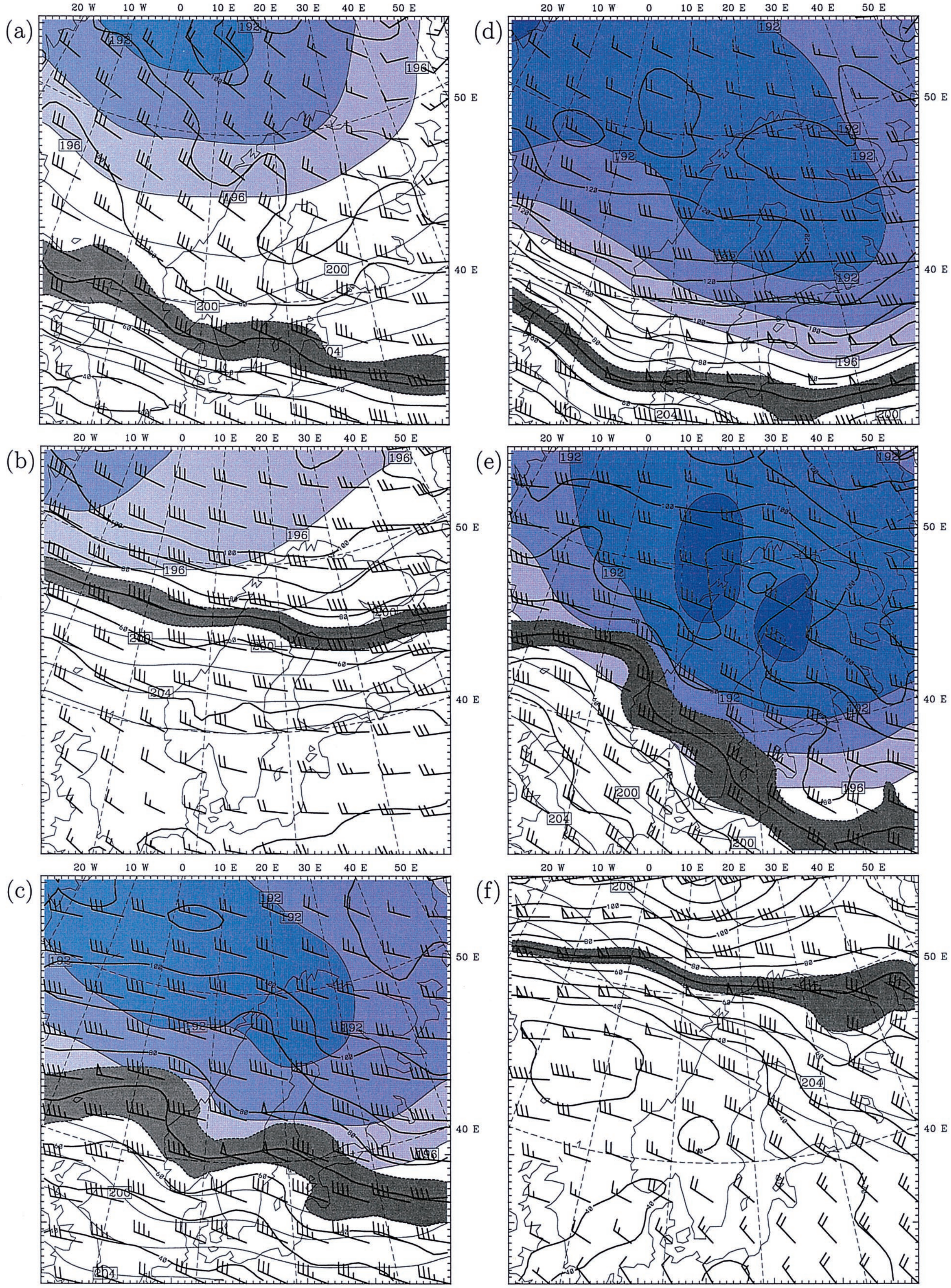

Plate 2. Synoptic-scale evolution of the stratosphere above Scandinavia in January 1997. ECMWF-analyzed temperature (in kelvins; shaded), horizontal wind vectors (barbs, in m s^{-1}), and potential vorticity (in 10^{-6} km^2 s^{-1} kg^{-1}) on the 550 K potential temperature surface at 1200 UT on January 4, 9, 14, 18, 22, and 26, 1997 (Plates 2a–2f, respectively), are shown.

not turn more than $\Delta\alpha_*$ from the wind direction at 900 hPa (see Figure 6):

$$\delta\alpha(p) = \alpha_H(p) - \alpha_H(900\ \text{hPa}) < \Delta\alpha_*$$

$$p = 500,\ 300,\ 100,\ 50\ \text{hPa}.$$

When all three criteria are satisfied, significant mountain waves are expected at stratospheric levels. In this way, the stratospheric mountain wave activity can be qualitatively parameterized by just two quantities (V_* and $\Delta\alpha_*$), the threshold value for the low-level wind speed V_* and the maximum wind turning $\Delta\alpha_*$. Note that $\Delta\alpha_*$ appears in different context: as the maximum possible deviation of the low-level wind direction from the normal of the mountain ridge (C2) and as the maximum wind turning from the low-level wind direction (C3). In this paper, the threshold values will be set to $V_* = 10$ m s^{-1} and $\Delta\alpha_* = 45°$. The impact of stronger constraints (larger V_*, smaller $\Delta\alpha_*$) on the stratospheric mountain wave activity is considered in the companion paper [*Dörnbrack and Leutbecher*, this issue].

Here, we apply the above criteria to a database of 6-hourly T106 L31 ECMWF synoptic-scale analyses of January 1997, whereby the horizontal wind speed V_H and the wind direction α_H are area averages on a surface of constant pressure over the control area Kebnekaise at a given time.

The temporal evolution of V_H and α_H for January 1997 is shown in Figure 7. For more than 58% of the time the low-level wind speed is larger than V_*. Maximum values occur during the stormy period January 21–22 (in gusts, more than 25 m s^{-1} were recorded; archived weather information, e.g., from the University of Tromsø, Norway, is available via internet at http://www.cs.uit.no/cgi-bin/weather). Most of the time, the low-level wind direction is nearly perpendicular to the mountain ridge. Frequently, the wind direction at stratospheric levels does not deviate largely from α_H (900 hPa).

Applying criteria C1, C2, and C3 to the synoptic-scale data as shown in Figure 7, a classification of synoptic-scale flow into periods of large and small stratospheric mountain wave activity ("bar code") can be generated (Figure 8). The last line of this code marks periods of stratospheric wave activity and can be thought of as a simple mountain wave parameterization. Figure 8 suggests good conditions for mountain wave excitation and propagation in at least three periods in January 1997: from January 9 till 11, from January 13 till 16, and from January 20 till 22. These periods coincide well with times when the minimum temperature anomaly ΔT is maximum (the shaded background in Figure 3). Thus it is confirmed that strong temperature deviations above Kebnekaise are caused by mesoscale gravity wave activity forced by the Scandinavian mountains.

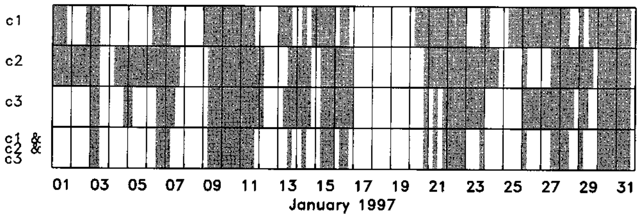

Figure 8. Classification indicating periods of significant mountain wave activity in the stratosphere. The criteria C1, C2, and C3 indicate periods when V_H (900 hPa) > 10 m s^{-1} (C1), when $255° < \alpha_H$ (900 hPa) $< 345°$ (C2), and when the directional shear between the wind direction at 900 hPa and every level of 500, 300, 100, and 50 hPa is less than 45°. In the last row, periods of stratospheric wave activity are marked when all conditions C1, C2, and C3 are satisfied simultaneously.

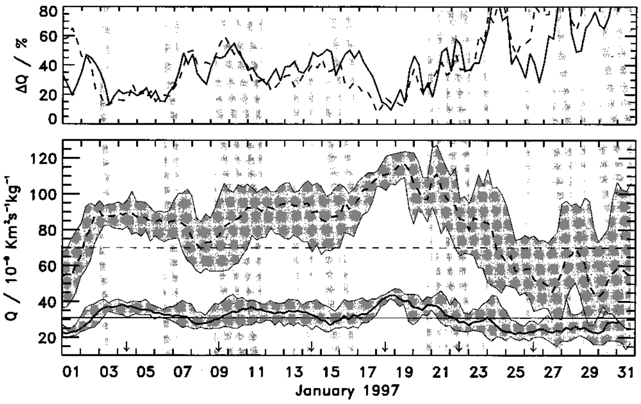

Figure 9. (top) Relative difference $\Delta Q = (Q^{\mathrm{T106}}_{\max} - Q^{\mathrm{T106}}_{\min})/\bar{Q}^{\mathrm{T106}}$ at 475 (solid line) and 550 K (dashed line) above northern Scandinavia inside the box with corner coordinates (3°, 30°) E and (54.25°, 71°) N. Data are from T106 ECMWF analyses. The shaded background areas indicate periods of stratospheric wave activity derived from the bar code in Figure 8. (bottom) Mean potential vorticity $\bar{Q}^{\mathrm{T106}}$ for both levels. Minimum and maximum values of Q in that area limit the shaded area. The edge of the polar vortex is indicated by typical values of 32 and 70×10^{-6} km^2 s^{-1} kg^{-1} for both levels, respectively. Vertical arrows point at dates for which horizontal sections are plotted in Plate 2.

Obviously, the criteria C1–C3 do not quantify the amplitude of the temperature perturbation as a function of height. If one wants to parameterize the mesoscale minimum temperature anomaly ΔT quantitatively, the Froude number $\mathcal{F} = U/Nh$ (U and N are the mean upstream wind speed and the buoyancy frequency of the low-level flow, respectively, and h is the mountain crest height) as well as the change of wind speed and thermal stability as a function of height must be taken into account.

6. Discussion: Position of the Stratospheric Polar Vortex

Generally, the evolution of the Arctic stratospheric winter 1996–1997 was unique: The polar vortex formed late in December 1996 and dissipated not before April 1997 [*Coy et al.*, 1997]. This long duration led to anomalously low ozone values above the Northern Hemisphere [*Newman et al.*, 1997]. For this study, the period January 1997 was chosen because alternating cooling and warming events reflect essential features of polar vortex dynamics during most of the winter seasons. In this section, we discuss the relationship between regions of cold stratospheric air, the position of the polar vortex above northern Scandinavia, and stratospheric mountain wave activity.

Plate 2 shows the synoptic-scale temperature distribution, horizontal wind, and potential vorticity deduced from ECMWF analyses on the 550 K isentropic surface for six selected times starting on January 4, 1997, 1200 UT. Figure 9 depicts the mean potential vorticity $\bar{Q}^{\mathrm{T106}}$ at 475 and 550 K averaged over the area of Scandinavia as shown in Figure 1. As maximum potential vorticity is always found at the northern boundary of the domain during January 1997, the normalized difference between the maximum and minimum value $\Delta Q = (Q_{\max}^{\mathrm{T106}} - Q_{\min}^{\mathrm{T106}})/\bar{Q}^{\mathrm{T106}}$ measures the north-south gradient of potential vorticity in that area (Figure 9).

At the beginning of the month the polar vortex encloses cold air and expands southward resulting in increasing potential vorticity (see Figure 9) and decreasing temperature (see Figure 2) above northern Scandinavia. On January 4 (Plate 2a) the edge of the polar vortex (in Plate 2 fixed as a potential vorticity belt of $70 \pm 5 \times 10^{-6}$ Km^2 s^{-1} kg^{-1}; see *Dameris et al.* [1995]) reached its southernmost extension. Afterward, the vortex moves northward until January 8–9 (Plate 2b). During the preceding and the following few days, northern Scandinavia is under the influence of the vortex edge. In the following period (Plates 2c and 2d) the vortex core and the associated cold air spread southward again and cover northern Scandinavia entirely on January 18. On this day, maximum values of $\bar{Q}^{\mathrm{T106}}$ (Figure 9) and a minimum mass flux (Figure 5) are achieved. It is interesting to note that during this period of low mountain wave activity (Figure 8) and minimum synoptic-scale temperatures at the 50 and 30 hPa levels (Figure 2) a PSC of type Ib was observed on January 19 (Plate 1) that is indicative for synoptic-scale cooling below the condensation temperature of supercooled ternary solution within the polar vortex [see *Mehrtens and Reichardt*, 1998].

The characteristic feature of the following evolution is a stationary cold region located above northern Scandinavia whereas the polar vortex returns northward. Therefore the core of the polar vortex becomes displaced from the cold air (see January 22, Plate 2e). This particular state of stratospheric flow is terminated by a sudden warming whereby the Arctic vortex disappeared off the domain in just 4 days (see January 26, Plate 2f).

Lidar measurements during the recent Arctic winters at Eureka (80°N, 86°W) by *Whiteway et al.* [1997] give evidence that maximum stratospheric wave activity is strongly correlated with a westerly jet at the edge of the polar vortex. Here, periods without stratospheric mountain wave activity (e.g., January 3–5 and 17–20) are characterized by large $\bar{Q}^{\mathrm{T106}}$ values and by small ΔQ (Figure 9). During these phases, northern Scandinavia is located beneath the center of the Arctic polar vortex. In contrast, periods of stratospheric wave activity are associated with smaller $\bar{Q}^{\mathrm{T106}}$ values but with large tendencies. Furthermore, large values of ΔQ indicate the edge of the polar vortex with marked north-south gradients of potential vorticity.

Before and after the interval of maximum $\bar{Q}^{\mathrm{T106}}$ (January 17–20), mountain wave–induced ice PSCs were observed by lidars at Esrange (Plate 2). In both periods a state of the stratospheric flow evolved, wherein at the inner edge of the polar vortex, high westerly winds and cold synoptic-scale temperatures coincided. Simultaneously, strong low-level winds excited gravity waves, which propagated without any significant absorption up to stratospheric levels, i.e., optimum conditions for extra mountain wave cooling. A similar pattern evolved in the well-documented period around January 9 [*Dörnbrack et al.*, 1998; *Wirth et al.*, 1999].

7. Summary

The results of this paper can be summarized as follows:

1. Conditions for significant mountain wave influence on the stratospheric temperature field are deduced and expressed as criteria C1, C2, and C3 in section 5. Periods of stratospheric mountain wave activity according to C1, C2, and C3 are diagnosed if strong low-level winds are nearly perpendicular to the mountain ridge while the wind direction does not turn significantly with height. These conditions agree with historic observations of orographically induced PSCs by *Störmer* [1931, 1934] and more recent measurements by *Whiteway and Duck* [1999], who found enhanced stratospheric gravity wave activity under conditions of small directional shear and large wind speed at the ground and above. Enhanced wave activity results in mesoscale stratospheric temperature anomalies of up to $\Delta T \approx 8$ K with respect to synoptic-scale conditions. Mesoscale temperature anomalies are located directly above as well as up to 500 km downstream of the Scandinavian mountain range (section 3).

2. Simulated mesoscale temperatures agree very well with radiosonde observations at different stratospheric levels for the entire January 1997 (section 3). Even the record minimum temperature of −94.5°C on January 22, 1997, is well represented by the numerical model [see also *Dörnbrack et al.*, 1999]. Large horizontal temperature differences of up to 20 K inside an area of 450 km × 450 km are the result of hydrostatic mountain waves and are not resolved in global circulation models. The insufficient spatial resolution of such models on the one side and the sparse stratospheric observations of ΔT on the other side usually underestimate the influence of mountain wave–induced temperature anomalies on the PSC formation. Mesoscale modeling provides a reliable data set resolving the mountain wave signature on the meso-β-scale of atmospheric motion [*Orlanski*, 1975].

3. Mesoscale minimum temperatures associated with mountain wave activity reach lower values for longer times compared with their synoptic-scale counterparts. Hence mountain waves considerably enlarge the potential for forming ice PSC particles. In January 1997, synoptic-scale temperature never fell below the frost point T_{frost}; however, mesoscale temperatures fell as low as that in three periods.

4. Microphysical calculations need reliable estimates of the additional amount of air that is actually processed by heterogeneous reactions due to mesoscale activity. This issue has been investigated by using trajectory analyses and calculating the associated mass flux in a control volume above the highest mountains. For periods when there is no processing due to the synoptic-scale flow (i.e., $T > T_{\mathrm{NAT}}$), up to 20% of the total mass flux can be processed on the mesoscale.

5. In accordance with recent lidar observations [*Whiteway et al.*, 1997] we found marked stratospheric temperature fluctuations correlated with the position of the edge of the Arctic polar vortex over northern Scandinavia. The largest mesoscale temperature anomalies are found when synoptically cold air is displaced from the center of the vortex and is influenced by the polar night jet, i.e., near the inner edge of the polar vortex (section 6).

In order to study the ozone budget of the Northern Hemisphere it is currently not possible to run a mesoscale model at horizontal resolutions of 15 km for entire winters. Therefore it seems likely that parameterizations remain the only means to estimate the effect of mountain waves on the hemispheric ozone budget [e.g., *Carslaw et al.*, 1999; *Bacmeister et al.*, 1999]. Such parameterizations need to be designed carefully to yield realistic wave amplitudes and realistic volumes affected by a wave-induced temperature anomaly. Otherwise the mass flux of air processed by heterogeneous reactions will be grossly incorrect.

A way of designing a reliable parameterization would be to compare it to the mass flux data presented in this study. In such a test the parameterization should attempt to resolve the same spectrum of orographic gravity waves. This could be done by using a similar orography. In such a setup the parameterization should yield similar values of the mass flux of processed air for a range of threshold values in the vicinity of the synoptic-scale temperature.

Acknowledgments. This work was supported by the BMBF in the framework of the German Ozone Research Programme. It is our pleasure to explicitly acknowledge the permission from B. Kuo (NCAR, Boulder, Colorado) to apply the MM5 model and the generosity of E. Kyrö and R. Kivi (Finnish Meteorological Institute, Sodankylä) for making available their high-resolution sounding data.

References

Bacmeister, J. T., P. A. Newman, B. L. Gary, and K. R. Chan, An algorithm for forecasting mountain wave-related turbulence in the stratosphere, *Weather Forecasting*, *9*, 241–253, 1994.

Bacmeister, J. T., S. D. Eckermann, A. Tsias, K. S. Carslaw, and T. Peter, Mesoscale temperature fluctuations induced by a spectrum of gravity waves: A comparison of parameterizations and their impact on stratospheric microphysics, *J. Atmos. Sci.*, *56*, 1913–1924, 1999.

Browell, E. V., C. F. Butler, S. Ismail, P. A. Robinette, A. F. Carter, N. S. Higdon, O. B. Toon, M. R. Schoeberl, and A. F. Tuck, Airborne lidar observations in the wintertime arctic stratosphere, 1, Polar stratospheric clouds, *Geophys. Res. Lett.*, *17*, 385–388, 1990.

Carslaw, K. S., et al., Increased stratospheric ozone depletion due to mountain-induced atmospheric waves, *Nature*, *391*, 675–678, 1998a.

Carslaw, K. S., M. Wirth, A. Tsias, B. P. Luo, A. Dörnbrack, M. Leutbecher, H. Volkert, W. Renger, J. T. Bacmeister, and T. Peter, Particle microphysics and chemistry in remotely observed mountain polar stratospheric clouds, *J. Geophys. Res.*, *103*, 5785–5796, 1998b.

Carslaw, K. S., T. Peter, J. T. Bacmeister, and S. D. Eckerman, Widespread solid particle formation by mountain waves in the Arctic stratosphere, *J. Geophys. Res.*, *104*, 1827–1836, 1999.

Coy, L., E. R. Nash, and P. A. Newman, Meteorology of the polar vortex: Spring 1997, *Geophys. Res. Lett.*, *24*, 2693–2696, 1997.

Dameris, M., M. Wirth, W. Renger, and V. Grewe, Definition of the polar vortex edge by lidar data of the stratospheric aerosol: A comparison with values of potential vorticity, *Beitr. Phys. Atmos.*, *68*, 113–119, 1995.

Dietrichs, H., Über die Entstehung der Perlmutterwolken, *Meteorol. Rundsch.*, *3*, 208–213, 1950.

Dörnbrack, A., Turbulent mixing by breaking gravity waves, *J. Fluid Mech.*, *375*, 113–144, 1998.

Dörnbrack, A., M. Leutbecher, H. Volkert, and M. Wirth, Mesoscale forecasts of stratospheric mountain waves, *Meteorol. Appl.*, *5*, 117–126, 1998.

Dörnbrack, A., M. Leutbecher, R. Kivi, and E. Kyrö, Mountain wave induced record low stratospheric temperatures above northern Scandinavia, *Tellus Ser. A*, *51*, 951–963, 1999.

Dörnbrack, A., and M. Leutbecher, Relevance of mountain waves for the formation of polar stratospheric clouds over Scandinavia: A 20 year climatology, *J. Geophys. Res.*, this issue.

Dudhia, J., A non-hydrostatic version of the Penn State-NCAR Mesoscale Model: Validation tests and simulation of an Atlantic cyclone and cold front, *Mon. Weather Rev.*, *121*, 1493–1513, 1993.

Gaffen, D. J., Temporal inhomogeneities in radiosonde temperature records, *J. Geophys. Res.*, *99*, 3667–3676, 1994.

Gary, B. L., Observational results using the microwave temperature profiler during the airborne Antarctic ozone experiment, *J. Geophys. Res.*, *94*, 11,223–11,231, 1989.

Grell, G. A., J. Dudhia, and D. R. Stauffer, A description of the fifth-generation Penn State/NCAR mesoscale model (MM5), *Tech. Note 398*, 121 pp., Natl. Cent. for Atmos. Res., Boulder, Colo., 1994.

Hanson, D., and K. Mauersberger, Laboratory studies of the nitric acid trihydrate: Implications for the south polar stratosphere, *Geophys. Res. Lett.*, *15*, 855–858, 1988.

Harris, N. R. P., I. Kilbane-Dawe, and G. T. Amanatidis (Eds.), *Polar Stratospheric Ozone*, *Proceedings of the 4th European Symposium on Polar Stratospheric Ozone*, *Schliersee*, *1997*, *Air Pollut. Res. Rep. 66*, *EUR 18032 EN*, Eur. Comm., Brussels, 1998.

Kivi, R., et al., SAONAS activities at Sodankylä in winter 1996/1997, in *Proceedings of the 4th European Symposium on Polar Stratospheric Ozone*, *Schliersee*, *1997*, *Air Pollut. Res. Rep. 66*, *EUR 18032 EN*, pp. 135–138, Eur. Comm., Brussels, 1998.

Knudsen, B. M., Accuracy of Arctic stratospheric temperature analyses and the implication for the prediction of polar stratospheric clouds, *Geophys. Res. Lett.*, *23*, 3747–3750, 1997.

Leutbecher, M., and H. Volkert, The propagation of mountain waves into the stratosphere: Quantitative evaluation of three-dimensional simulations, *J. Atmos. Sci.*, *57*, 3090–3108, 2000.

Mehrtens, H., and J. Reichardt, Particle properties of a PSC observed on January 19, 1997 above Andoya and Esrange, in *Proceedings of the 4th European Symposium on Polar Stratospheric Ozone*, *Schliersee*, *1997*, *Air Pollut. Res. Rep. 66*, *EUR 18032 EN*, pp. 147–150, Eur. Comm., Brussels, 1998.

Mohn, H., Irisierende Wolken, *Meteorol. Z.*, *10*, 81–97, 1893.

Müller, K.-P., G. Baumgarten, J. Siebert, and K.-H. Fricke, PSC observations with the new lidar facility at Esrange, Kiruna in winter 1996/1997, in *Proceedings of the 4th European Symposium on Polar Stratospheric Ozone*, *Schliersee*, *1997*, *Air Pollut. Res. Rep. 66*, *EUR 18032 EN*, pp. 155–158, Eur. Comm., Brussels, 1998.

Newman, P. A., J. F. Gleason, R. D. McPeters, and R. S. Stolarski, Anomalously low ozone over the Arctic, *Geophys. Res. Lett.*, *24*, 2689–2692, 1997.

Orlanski, I., A rational subdivision of scales for atmospheric processes, *Bull. Am. Meteorol. Soc.*, *56*, 527–530, 1975.

Pawson, S., B. Naujokat, and K. Labitzke, On the polar stratospheric cloud formation potential of the northern stratosphere, *J. Geophys. Res.*, *100*, 23,215–23,225, 1995.

Peter, T., Microphysics and heterogeneous chemistry of polar stratospheric clouds, *Annu. Rev. Phys. Chem.*, *48*, 785–822, 1997.

Poole, L. R., and M. P. McCormick, Airborne lidar observations of Arctic polar stratospheric clouds: Indications of two distinct growth stages, *Geophys. Res. Lett.*, *15*, 21–28, 1988.

Queney, P., The problem of airflow over mountains: A summary of theoretical studies, *Bull. Am. Meteorol. Soc.*, *29*, 16–27, 1948.

Reichardt, J., U. Wandinger, M. Serwazi, and C. Weitcamp, Combined Raman lidar for aerosol, ozone, and moisture measurements, *Opt. Eng.*, *5*, 1457–1465, 1996.

Schreiner, J., C. Voigt, A. Kohlmann, F. Arnold, K. Mauersberger, and N. Larsen, Chemical analysis of polar stratospheric cloud particles, *Science*, *283*, 968–970, 1999.

Stein, B., et al., Optical classification, existence temperatures, and coexistence of different polar stratospheric cloud types, *J. Geophys. Res.*, *104*, 23,983–23,993, 1999.

Störmer, C., Höhe und Farbverteilung der Perlmutterwolken, *Geofys. Publ.*, *IX*, 3–25, 1931.

Störmer, C., Höhenmessungen von Stratosphärenwolken, *Beitr. Phys. Atmos.*, *21*, 1–6, 1934.

Whiteway, J. A., and T. J. Duck, Evidence for critical level filtering of atmospheric gravity waves, *Geophys. Res. Lett.*, *23*, 145–148, 1996.

Whiteway, J. A., and T. J. Duck, Enhanced Arctic stratospheric gravity wave activity above a tropospheric jet, *Geophys. Res. Lett.*, *26*, 2453–2456, 1999.

Whiteway, J. A., T. J. Duck, D. P. Donovan, J. C. Bird, S. R. Pal, and A. I. Carswell, Measurements of gravity wave activity within and around the Arctic stratospheric vortex, *Geophys. Res. Lett.*, *24*, 1387–1390, 1997.

Wirth, M., A. Tsias, A. Dörnbrack, V. Weiß, K. S. Carslaw, M. Leutbecher, W. Renger, H. Volkert, and T. Peter, Model guided Lagrangian observation and simulation of mountain polar stratospheric clouds, *J. Geophys. Res.*, *104*, 23,971–23,981, 1999.

G. Baumgarten and K.-P. Müller, Physikalisches Institut des Universität Bonn, Nussallee 12, D-53115 Bonn, Germany.

A. Behrendt and J. Reichardt, GKSS Forschungszentrum, Postfach 1160, D-21494 Geesthacht, Germany.

A. Dörnbrack and M. Leutbecher, Institut für Physik der Atmosphäre, DLR Oberpfaffenhofen, D-82230 Wessling, Germany. (andreas.doernbrack@dlr.de)

(Received April 23, 1999; revised March 8, 2000;
accepted March 14, 2000.)